Final Report

USGS Award Number G19AP00060

Determining Accurate Focal Depths and Seismic Moments of Small CEUS Earthquakes Using Only Regional Seismic Network Data

By Nawa R. Dahal and John E. Ebel (Principal Investigator)
Weston Observatory
Department of Earth and Environmental Sciences
Boston College
381 Concord Rd.
Weston, MA 02493 USA

John E. Ebel -- tel.: 617-552-8319; fax: 617-552-8388; email: ebel@bc.edu
Nawa R. Dahal -- tel.: 617-552-8300; fax: 617-552-8388; email: dahaln@bc.edu

Prepared
5 August 2020

Award Dates
1 June 2019 to 31 May 2020

This material is based upon work supported by the U.S. Geological Survey under Grant No. G19AP00060. The views and conclusions contained in this document are those of the authors and should not be interpreted as representing the opinions or policies of the U.S. Geological Survey.

ABSTRACT

Determinations of the source parameters of earthquakes are important to help understand the seismogenic structures such as faults that could be the potential seismic source zones of future strong earthquakes. The source parameters of small earthquakes recorded by a sparse regional seismic network are usually poorly constrained, and this is the case for many earthquakes in the Central and Eastern United States (CEUS). Dahal and Ebel (2019, 2020) proposed methods to find the focal depths, moment magnitudes and focal mechanisms of earthquakes with magnitudes between M4.0 and M2.5 recorded by a sparse seismic network. Their method analyzes the envelope functions of the seismic waveforms using synthetic waveform envelopes to search for the source parameters. In this study, we have analyzed 28 earthquakes of M3.7-M2.3 from the CEUS and constrained their source parameters using the Dahal and Ebel (2019, 2020) method. The source parameters obtained in this study are compared to those obtained using routine hypocentral determinations from regional network P and S arrival times for the focal depth and from moment tensor inversions for the focal mechanism and seismic moments whenever available. The focal depths obtained in this study are usually shallower than those obtained from routine hypocentral locations from P and S arrival times, but are comparable to the depths obtained from the moment-tensor inversion results that are available. Of the 28 earthquakes analyzed, the moment magnitudes for 26 of the events are determined for the first time, and 16 earthquakes had reliable focal mechanism determinations, of which only 2 events had previously-reported focal mechanisms. The focal depths of the earthquakes analyzed in this study ranged from 2-15 km with a majority of the depths being less than 5 km. The moment magnitudes of the earthquakes ranged from M_w2.7-3.7. The focal mechanisms ranged from oblique thrust faulting to oblique normal faulting.

INTRODUCTION

The CEUS exhibits low-to-moderate seismic hazard with the number of regional seismic network (RSN) centers diminishing over the past two decades (Ebel et al., 2020). Following the deployment of the EarthScope Transportable array and the adoption of approximately one-quarter of those stations for incorporation into the RSNs of the region in 2015, the number of RSN stations available to record earthquakes in the CEUS has changed little. In a few areas like the New Madrid Seismic Zone there is a dense concentration of RSN stations, which allows precise hypocenters and focal mechanisms to be computed for many of the small earthquakes that routinely take place. However, for large areas of the CEUS the average RSN station spacing today is about 50-100 km, which makes the task of constraining the source parameters of the regional and local earthquakes occurring in this area difficult, as the sparse seismic network does not provide adequate data for the computation of reliable focal depths. In addition, the lack of a dense azimuthal coverage of RSN stations at close epicentral distances such that unequivocal P first-motion directions can be read limits the computation of reliable focal mechanisms only to those events large enough for regional moment-tensor inversions. Thus, for almost all CEUS events less than about M_w3.5-4.0, well-constrained focal depths and focal mechanisms are not being determined today.

Determining accurate source parameters of small earthquakes in the CEUS is important for better constraining the potential seismic source zones of an area like the CEUS and for estimating the possible locations of future large earthquakes. The recent study entitled *Central and Eastern United States Seismic Source Characterization for Nuclear Facilities* (CEUS SSC, 2012) looked in great detail at all of the issues needed to characterize the seismic source zones of the CEUS. Among its findings, CEUS SSC (2012) indicated that focal mechanisms and seismic moments of small earthquakes are necessary to identify seismically active structures and to properly constrain the sizes of the small earthquakes. The latter is important because the recurrence estimates of large earthquakes relies on the statistics of the more-frequent smaller earthquakes, but the moment magnitudes of the smaller earthquakes (below about M_w4.0) at present must be estimated using conversions from other, often heterogeneous magnitude scales. The direct determination of moment magnitudes for all smaller earthquakes in a region like the CEUS is required to reduce the uncertainties in the recurrence estimates of large magnitude events.

Another significant problem in current earthquake catalogs for the CEUS that adds uncertainties to seismic hazard computations is that earthquake focal depths are poorly determined for most earthquakes in the CEUS because of the relatively sparse seismic station coverage in many parts of the region (CEUS SSC, 2012). Fortunately, for earthquakes above about $M_w \geq 4.0$ moment-tensor inversions using broadband regional seismic waveforms allow the determinations of accurate focal depths (see the website of R. Herrmann website listed in Data and Resources; Guilhem et al., 2014). Unfortunately, too often it is difficult to constrain the focal depths of smaller earthquakes due to the sparse local broadband regional seismic station coverage in much of the CEUS. Seismologists really have only two choices to tackle this issue. One is to find significant new funding to greatly increase the number of seismic stations operating throughout the region, something that is not likely to happen anytime soon. The other is to test new data analysis methods that can be used to better analyze the existing regional seismic network recordings of the smaller ($M_w \leq 4.0$) earthquakes that take place regularly in the CEUS. It is this latter approach that we followed in this project.

For the past two decades or so, one method for determining seismic source information (moment tensor, seismic moment, and focal depth) for earthquakes of $M_w \geq 4.0$ has involved inversions of filtered versions of full event waveforms at regional distances from an earthquake epicenter. These methods were developed based on early work such as that of Dreger and Helmberger (1993), Zhao and Helmberger (1994) and Zhu and Helmberger (1996). The most common method for computing seismic source information using regional waveforms is the one developed by Doug Dreger (Dreger, 2008). That method works very well for earthquakes above $M_w 4.0$ with data at epicentral distances from a few to several hundred kilometers. Unfortunately, the method is designed to work with seismic energy at frequencies below about 0.10 Hz, and the signals in this frequency band are very difficult or impossible to observe if the earthquake is smaller than about $M_w 3.5$-4.0. Dahal and Ebel (2019, 2020) designed a waveform inversion method based on the analysis of the envelopes of filtered, broadband earthquake signals that could resolve the earthquake focal depth for events as small as $M_w 2.5$ using the waveforms from one or just a few regional seismic stations. Furthermore, they showed that their method could find reliable earthquake focal mechanisms for earthquakes of down to $M_w 3.0$ and sometimes even somewhat smaller, again using the waveforms from just a few regional seismic stations. It is their method that we applied in this study is to extend the regional moment tenor computations to magnitudes as low as $M_w 2.5$ for events in the CEUS. We show in this study that the Dahal and Ebel (2019, 2020) method works well for small earthquakes throughout the CEUS.

DATA

Event origin time, station epicentral distance, station azimuth, station network code, event magnitude, station name and the seismograms were read from the IRIS wilber3 system for each event and each station included in this study. We selected earthquakes from 2011 to 2019 using the earthquake search tool of the Advanced National Seismic System, the details of which are presented in Table 1. We analyzed 28 earthquakes with magnitudes less than M4.0 and with epicenters from Quebec, Canada in the northeast to Oklahoma, USA in the southwest. To ensure analysis of events from all important seismically active areas in the CEUS we included earthquakes from the New Madrid and Eastern Tennessee seismic zones. All the events analyzed in this study along with the locations of the stations used in our analyses are shown in Figure 1.

The Green's functions utilized in the analysis were generated using the frequency-wavenumber integration code FKRPROG.f, which is based on Saikia (1994). The Green's functions were generated at a grid of epicentral distances and source focal depths with epicentral distances ranging from 20-450 km at a step of 5 km and with depths at each epicentral distance ranging from 1 to 20 km at a step of 1 km. We generated Green's functions by utilizing the crustal models (1-D flat earth model) published on R. Herrmann's website listed in the Data and Resources section and listed in Table 2 for Events 1-5 in Table 1 and listed in Table 3 for the rest of the events in Table 1. Synthetic seismograms were calculated for focal mechanisms with dip from 0^o to 90^o and rake and strike both from 0^o to 360^o, all varying at a step of 10^o for the determination of the focal depth and the moment magnitude, while the dip/rake/strike angles were all varied at a step of 30^o for the determination of the focal mechanism. Moment tensor components were calculated using Equation (18) of Jost et al. (1989) with selected values of strike, dip, rake and scalar moment as inputs. With our Green's functions, our scalar seismic moment and our moment tensor components, we calculated synthetic seismograms using equations (A5.4), (A5.5) and (A5.6) in Appendix V of Jost et al. (1989). Both the observed seismograms as well as the Green's functions were filtered forward and backward through a Butterworth bandpass filter with 2 poles and a passband of 1.0-3.0 Hz for the determinations of the focal depths and moment magnitudes and through a bandpass of 1.5-2.5 Hz for the determinations of the focal mechanisms. A minimum of 1 station and a

maximum of 6 stations per event each with SNR above 5 were used for the determination of the focal depth and moment magnitude while a minimum of 3 stations and a maximum of 6 stations per event each with SNR above 10 were used for the determination of the focal mechanisms. The epicentral distances of the stations used in our analyses ranged from 39-338 km.

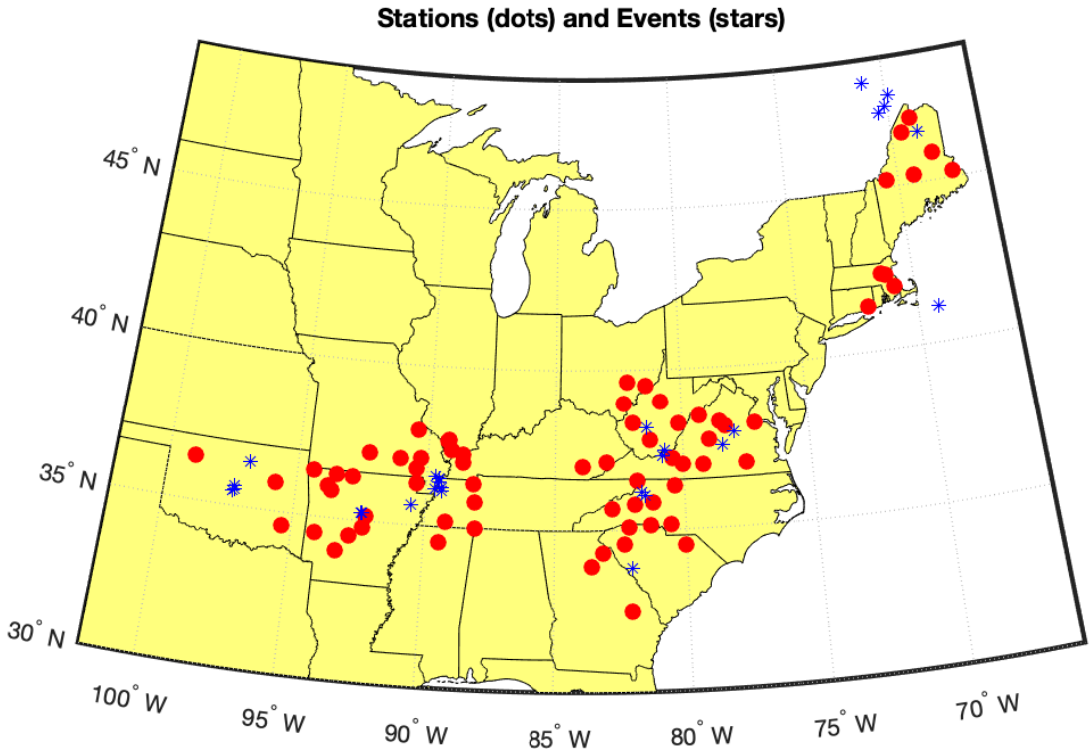

Fig 1. Map showing the events analyzed in this study along with the stations used in the analyses.

Table 1: List of the Events Analyzed in this Study

Event Number	Date yyyy/mm/dd	Time UTC hh:mm:ss	Lat. (°N)	Lon. (°W)
1	2019/11/15	04:14:48	48.276	71.014
2	2019/11/02	13:43:07	47.835	69.897
3	2019/08/29	12:12:47	47.303	70.434
4	2019/08/31	13:47:52	47.476	70.123
5	2019/09/25	02:06:01	46.573	68.837
6	2018/08/18	21:21:27	41.130	69.127
7	2013/08/25	19:50:40	36.165	81.664
8	2014/12/15	06:44:16	36.059	81.520
9	2014/02/16	20:23:35	33.830	82.066
10	2017/09/13	17:33:10	37.473	80.703
11	2017/06/21	08:01:32	38.200	81.399
12	2017/05/12	04:31:10	37.277	80.841
13	2015/11/04	11:00:52	37.563	78.431
14	2015/03/15	07:02:35	37.961	77.953
15	2019/10/12	13:55:25	36.555	89.648
16	2017/08/15	13:59:01	36.393	89.530
17	2013/07/17	20:10:33	35.625	90.564
18	2013/01/07	18:29:13	36.224	89.436
19	2012/09/03	12:12:32	36.490	89.546
20	2020/02/04	05:35:46	36.105	89.416
21	2016/11/24	01:57:37	36.155	89.693
22	2011/03/22	19:56:05	35.250	92.403
23	2011/03/17	17:59:47	35.242	92.399
24	2011/03/24	07:38:59	35.245	92.368
25	2016/09/03	15:25:00	35.599	97.345
26	2013/01/17	00:53:26	36.413	96.858
27	2013/03/21	15:56:41	35.492	97.312
28	2013/03/21	16:34:35	35.467	97.396

Table 2: Crustal Model Taken from R. Herrmann's Website (as indicated in Data and Resources) to Generate the Green's Functions for Events 1-5 in Table 1.

Thickness (km)	Vp (km/s)	Vs (km/s)	Rho (g/cc)	1/Qp	1/Qs
1.9	3.41	2.01	2.22	331	147
6.1	5.55	3.30	2.61	287	128
13	6.27	3.74	2.78	472	210
19	6.41	3.77	2.82	901	411
-	7.90	4.62	3.28	6098	2703

Table 3: Crustal Model Taken from R. Herrmann's Website (as indicated in Data and Resources) to Generate the Green's Functions for Events 6-28 in Table 1.

Thickness (km)	Vp (km/s)	Vs (km/s)	Rho (g/cc)	1/Qp	1/Qs
1	5	2.89	2.50	581	258
9	6.10	3.52	2.73	625	275
10	6.40	3.70	2.82	671	298
20	6.70	3.87	2.90	9000	5000
-	8.15	4.70	3.36	515	232

METHOD

Our waveform-envelope fitting method is carried out in two iterative steps. The first step is to perform a coarse grid search over all possible dip, rake and strike angles and as well as over possible depths and scalar moments. The second step is then to find the optimal solution utilizing the solution from the grid search. A summary of the method is presented in the following 4 steps:

1) Background Preparation: The first step is to select a set of the stations, a frequency passband, a range of seismic moments, a range of source focal depths and the steps in dip/rake/strike angles to be used in the analysis as well as to generate a set of Green's functions for the desired range of source depths and epicentral distances. Stations with SNR higher than a threshold SNR for a given frequency passband are chosen to be included in the analysis. A threshold SNR is predetermined at different epicentral distances for different magnitude events and different passband frequencies used. The range of seismic moments is chosen based on the magnitude of the event whereas the range of focal depths is selected based on the prior knowledge about the capacity of the study area to host earthquakes of different depths.

2) Data Processing: In the second step, the regional waveforms are read/downloaded from where they are stored (e.g., IRIS DMC), the seismogram amplitudes are normalized to ground velocity, any DC amplitude shift present in the data is removed, all three components are aligned at the same starting time and are rotated to the radial, tangential and the vertical directions. Following that, the velocity components are integrated to ground displacements, tapered at the beginning and at the end to prevent a step response from filtering, forward and reverse filtered to avoid any phase shifts from filtering, resampled to the sampling frequency to which the Green's functions are calculated and finally converted to their envelopes using the

Hilbert transform. The Green's functions are filtered and processed exactly in the same manner as the observed waveforms and are into synthetic seismograms by combining with the moment tensor components and a given value of scalar moment before they are converted to the envelopes.

3) Coarse Grid Search: The observed envelopes for a seismic station and each set of possible synthetic envelopes (as determined by the steps in dip, rake and strike angles) for a given depth for that station are crosscorrelated to find the optimal time shift, i.e. the time shift that yields the highest value of crosscorrelation coefficient. The traces are then aligned at the optimal shift and the fit of the synthetic envelopes to the observed envelopes is calculated in terms of modified variance reduction (MVR). The synthetic envelope with the largest MVR value for that depth from among all of the stations is found. The process is repeated for a desired range of depths and a desired range of scalar moments until we find the optimal value of the depth and the optimal value of the scalar moment for the given event. MVR is calculated as defined in the equation below:

$$MVR = [1 - \frac{(\sum_i w_i \sum_j (d_{ij} - sij)^2)}{\sum_i w_i \sum_j [(d_{ij})^2 + (s_{ij})^2]}] \times 100\%$$

where the subscripts 'i' refers to the station number and the subscript 'j' refers to one of the three data components. 'd' is the observed seismogram. 's' is the synthetic seismogram. 'w' is the weight given to each station so that the farther stations are weighted more. The inverse distance weighting scheme is used because as we are using the envelopes of the full waveforms, the higher amplitudes in the waveforms are controlled mostly by the surface waves and the surface waves become the more prominent seismic phases with epicentral distance.

4) Finding the Optimal Solution: The optimal solution is obtained either by doing a finer grid search around the optimal solution that was obtained from the coarse grid search or by carrying out an iterative non-linear inversion of the waveform envelopes using the optimal source parameters from the coarse grid search as the starting model.

RESULTS

Focal depths and moment magnitudes obtained for the events in NENA analyzed in this study using the method of Dahal and Ebel (2019, 2020) are presented in Table 4. Our depths ranged from 3-15 km for the events from Quebec, Canada (Events 1-4 in Table 4) and from 2-6 km for the events in the CEUS (rest of the events in Table 4). The depths reported in Table 4 from this study are obtained by using all the stations with SNR > 5 available for an event. The error in depth of an event is the standard deviation in the depths obtained by analyzing individually one station at a time for all the stations included in the analysis for that event. For the events analyzed in this study, the error in the depths ranged from less than 1 km to 7 km. The depths of all the events analyzed in this study as reported by the USGS are reported in Table 4, and the depths of these events as reported by Lamont Doherty Earth Observatory (LDEO), R. Herrmann's web site listed in Data and Resources, and the Canada Natural Resource Center (CNRC) are also listed in Table 4 whenever available. The depths reported on R. Herrmann's web site listed in Data and Resources are obtained from moment tensor inversion while the depths obtained by all the other institutions are obtained from a routine hypocentral

Table 4. Depths, Moment Magnitudes and Focal Mechanisms of the events analyzed in this study

S.N.	This Study				USGS			Kagan Angle (°)	Percentile for all Possible Rotations of Double-Couple Sources
	M_0 (10^{20} dyne-cm)	M_w	Depth (km)	(D°, R°, S°)	mb_lg	Depth (km)	(D°, R°, S°)		
1	10	3.3±0.2	4±7	60/120/120	3	19.1	--		
2	5	3.1±0.1	6±2	60/150/240	2.8 (ml)	14.8**(10)**	--		
3	5	3.1±0.1	3±1	60/0/120	3.16(M_w)	3.7**(6)[1]**	52/117/174	94	87
4	7	3.2±0.1	15±3	60/60/240	2.7	5.0**(10)**	--		
5	3.5	3.0±0.1	4±2	60/120/120	2.7	5 *(19.4)*	--		
6	1.3	2.7±0.2	4±7	--	2.4	5.0	--		
7	7	2.7±0.2	4±7	--	2.9 (md)	9.1	--		
8	5	3.1±0.1	3±0	60/120/300	3.0 (md)	13.2	--		
9	7	3.2±0.2	4±4	60/30/300	3.02 (M_w)	**[6.0]**	40/-172/256	47	23
10	30	3.6±0.1	3±0	60/210/150	3.2 (md)	17.8	--		
11	2	2.8±0.2	4±0	--	2.7 (md)	16.6*(5)*	--		
12	0.6	2.7±0.1	3±0	--	2.8 (md)	4.1	--		
13	1.3	2.8±0.2	4±4	--	2.6 (md)	7.5	--		
14	10	3.3±0.2	4±0	30/150/180	2.8 (md)	5.0	--		
15	15	3.4±0.2	4±0	60/300/90	3.3	9.7	--		
16	3.5	3.0±0.2	3±0	30/120/330*	2.9 (md)	8.9	--		
17	20	3.5±0.2	3±0	60/30/140	3.2 (md)	13.6	--		
18	05	3.1±0.0	3±3	60/60/210	2.6 (md)	6.3	--		
19	5	3.1±0.2	3±0	60/60/0	2.6	8.8	--		
20	5	3.1±0.1	3±0	60/0/150*	2.6	10.2	--		
21	40	3.7±0.2	3±1	60/120/120	3.3	8.8	--		
22	20	3.5±0.2	3±7	30/60/330	3.3	5.2	--		
23	5	3.1±0.3	3±0	60/0/30*	3.0 (md)	5.0	--		
24	7	3.2±0.1	3±2	60/30/30	2.8	3.8	--		
25	15	3.2±0.2	4±3	60/30/90*	2.8 (ml)	4.8	--		
26	1.3	2.7±0.1	2±1	--	2.9 (ml)	8.0	--		
27	40	3.7±0.0	5±0	--	3.3 (ml)	10.5	--		
28	10	3.5±0.1	4±7	--	3.2	5.0	--		

Depths in parenthesis with bold fonts are from Canada Natural Resources Site (CNRS). Depths in parenthesis with italic fonts are from Lamont Doherty Earth Observatory (LDEO). Moment magnitude (M_w) are from R. Herrmann's website indicated in Data and Resources. D°, R°, S° refer to the dip, rake and strike angles in degrees. '*' refers to two possible rake angles for the given focal mechanism; one that is indicated in Table 4 and the other 180° apart from what is indicated in Table 4. '--' refers to data unavailable.

calculation using station P and S arrival times in Hypoinverse or some similar program. Our depths are comparable to the depths obtained by moment-tensor inversion (events 4 and 9 in Table 4), whereas our depths are usually smaller as compared to the depths computed from routine hypocentral determination methods (the remaining events in Table 4).

Table 4 also lists the moment magnitudes for all the events analyzed in this study. The moment magnitudes reported from this study are obtained by analyzing the data from all available stations at the same time whereas the error in the magnitudes is the standard deviation calculated using the magnitudes obtained from analyzing the event waveforms from each station separately. The moment magnitudes obtained in this study ranged from M_w2.7-3.7 with the error always less than or equal to 0.2 magnitude units. The magnitudes from the USGS as obtained from their routine hypocentral determinations are reported for each event using one of several different magnitude scales (mb_lg, ml or mb), whereas the magnitudes reported on R. Herrmann's web site (listed in Data and Resources) obtained through moment-tensor inversion all are reported as M_w magnitudes. Two of the events we analyzed (Events 4 and 9 in Table 4) had previously reported moment magnitudes as published on R. Herrmann's web site (listed in Data and Resources). The previously reported moment magnitudes for both of these events fall within the error range of the moment magnitudes as obtained from this study. For all the remaining events in Table 4, we cannot make a direct comparison of the moment magnitudes we have obtained from our analyses because there are not previous moment magnitudes determined for these events. The error of 0.2 magnitude units or lower observed in the determination of M_w from this study is similar to the error range of 0.07-0.14 in the calculation of moment magnitudes using moment-tensor inversion in other studies (e.g., Duputel et al., 2014), whereas it is less than the error involved in estimating M_w using a conversion from other magnitude scale (Wheeler, 2014).

Our method has an inherent ambiguity in the slip direction on the fault as we are fitting envelopes of seismograms instead of the seismograms themselves (Dahal and Ebel, 2020). Our method yields two possible focal mechanisms for a single event which are 180^o apart in rake. The symmetry in the direction of the rake can be broken by observing the direction of the first P-arrival for at least one station. To decide which of the two mechanisms is the true mechanism, we observed the direction of the first P-arrival in the observed seismograms as well as in the synthetic seismograms for all available stations. Clear P arrivals from at least 1 station and at most 6 stations are utilized for the events in this study in deciding which of the two possible focal mechanisms is the true mechanism.

Of the 28 earthquakes analyzed in this study, 22 events have $M_w \geq 3.0$ and 20 events were recorded by at least 3 stations with SNR of 10 and greater. Given these conditions, we were able to constrain two possible focal mechanisms for 20 events. Out of these 20 events, we were able to find unique focal mechanisms for 16 events. For remaining 4 events, 3 events lacked clear first motion arrivals (Events 16, 20, and 25 in Table 4) and 1 event had an equal number of contradicting polarities when the polarities from the observed seismograms were compared to the polarities from the synthetic seismograms (Event 23 in Table 4).

Of the 16 events with unique focal mechanisms, 11 events have oblique thrust mechanisms and the remaining 5 events have oblique normal mechanisms. Only 2 events (Events 4 and 9 in Table 4) among the 16 events with unique focal mechanisms from this study had previously reported focal mechanisms from the USGS, which, in turn, had taken those focal mechanisms from R. Herrmann's web site (listed in Data and Resources). For Event 4, we obtained an oblique thrust mechanism like

that of R. Herrmann, but for Event 9, we obtained an oblique thrust mechanism as opposed to the oblique normal mechanism obtained by R. Herrmann. We have used the Kagan angle as a measure to compare two different focal mechanisms with each other. A double-couple source can be rotated into another arbitrary double-couple source through four possible rotations in a 3D space. The minimum angle of rotation among these four possible rotations is called the Kagan angle. A Kagan angle can vary from 0° to 120°, in which 0° represents exactly the same mechanisms and 120° represents totally different mechanisms (Kagan, 1992). Our focal mechanisms have a Kagan angle of 74^{o} and a Kagan angle of 47^{o} for Event 4 and event 9, respectively, as compared to the focal mechanisms of R. Herrmann for these events. The Kagan angle of 47^{o} falls within the 11th percentile and the Kagan angle of 75^{o} falls within the 44th percentile of all possible double-couple orientations. The focal mechanisms calculated using the method of this study are within the 12th percentile of all possible double couple orientations when the maximum azimuthal gap between the station used in the analysis is 128^{o} (Event 9 in Table 5) and is within 87th percentile of all possible double couple orientations when the maximum azimuthal gap is 324^{o} (Event 3 in Table 5) as compared with the focal mechanisms obtained through independent moment-tensor inversions by R. Herrmann

Dahal and Ebel (2019) filtered the waveforms that they analyzed through a Butterworth bandpass of 1.0-3.0 Hz to determine the focal depths and seismic moments whereas Dahal and Ebel (2020) filtered their waveforms through a frequency band of 1.5-2.5 Hz to determine the focal mechanisms of the events below M_w4.0. The main reason that Dahal and Ebel (2020) used the frequency band of 1.5-2.5 Hz for constraining the focal mechanisms was that this filter band provided the best fit of their synthetic envelopes with their observed envelopes for the events they worked with. We determined the focal mechanisms for the events in this study using both 1.5-2.5 Hz and 1.0-3.0 Hz, and we found that the envelopes most often produced a better fit when they were filtered through the frequency band of 1.0-3.0 Hz. This new set of finding came as we have tested the events in this study from a wider region (from Quebec to Oklahoma) as compared to the events tested by Dahal and Ebel (2019, 2020) which were primarily from Mineral, Virginia and Ladysmith, Quebec. Going from a frequency band of 1.0-3.0 Hz to 1.5-2.5 Hz, our fits increased for two events, Event 5 and Event 9 in Table 5, by 1.29% and 1.67%, respectively, while the fits decreased for all the other events for which we were able to determine a unique focal mechanism. The decrease in the fits ranged from 0.55% (for Event 21 in Table 5) to 31.79% (for Event 18 in Table 5). The Kagan angles for the focal mechanisms obtained in this study using the two frequency bands range from 0-98^{o}, all of which are within the 87th percentile when compared to the possible double-couple orientations with the majority of them within 4th percentile.

We selected events from different parts of CEUS and analyzed them for focal depths, moment magnitudes, and focal mechanisms using two different crustal structures to see how well our method worked throughout the CEUS. The crustal structure listed in Table 2 was used to analyze events in Quebec and Maine, which produced variance reductions always greater than 71.14% and less than 73.00%. The crustal structure listed in Table 3 was used to analyze events for rest of the events in this study, which ranged from MA in the northeastern CEUS to OK in the midwest. For events in MA, NC, WV and VA, the variance reductions are always greater than 53.95% and less than 72.94% with values less than 60% for only 1 out of 9 events. For events in TN, MO, AR and OK the variance reductions are between 53.14% and 70.87% with values greater than 60% for 2 out of 14 events. This indicates that the crustal structure used to generate the Green's functions for Quebec and Maine produced better fits than the crustal structure used to generate the Green's functions for the rest of the geographical regions included in this study. The crustal structure used to generate Green's functions from MA in the northeastern US to OK in the midwest produced better fits for events east of VA than for events west of VA. Despite the variation in the synthetic fits observed for different regions, our results for focal depths, moment magnitudes and focal mechanisms are comparable for all areas as indicated by the

errors involved in the calculation of focal depths and moment magnitudes and by the percentiles of the Kagan angles.

DISCUSSIONS AND CONCLUSIONS

We analyzed 28 events from NENA using the enveloping fitting method of Dahal and Ebel. Our depths ranged from 3-15 km for the events from Quebec (Events 1-4 in Table 4) and from 2-6 km for the events in CEUS with the error in the depths ranging from less than 1 km to 7 km. Our depths are comparable to the depths obtained from the available moment-tensor inversion results, whereas our depths are usually lower as compared to the depths computed from the routine hypocentral determinations from P and S arrival-time data. The moment magnitudes obtained in this study ranged from M_w 2.7-3.7 with the error always less than about 0.2 magnitude units. We constrained focal mechanisms for 16 events, out of which the focal mechanisms for 14 events of the events are reported in this study for the first time. Our moment magnitudes agree with the moment magnitudes obtained through other moment-tensor inversions whenever available, and we have determined moment magnitudes for 20 events for the first time. The focal mechanisms calculated using the method used in this study are within the 1st percentile of all possible double couple orientations when the maximum azimuthal gap between the station used in the analysis is 128^o and is within 22nd percentile of all possible double-couple orientations when the maximum azimuthal gap is 324^o as compared to the focal mechanisms obtained through independent moment-tensor inversions by R. Herrmann. This shows that azimuthal coverage is crucial in finding accurate focal mechanisms with our method.

Table 5. Focal Mechanisms of the Events Analyzed in this Study

S.N.	(D^o, R^o, S^o) Obtained Using 1.0-3.0 Hz	MVR (%) in 1.0-3.0 Hz	(D^o, R^o, S^o) Obtained Using 1.5-2.5 Hz	MVR (%) Using 1.5-2.5 Hz	Kagan Angle (^{o}) between Focal Mechanisms Obtained Using 1.0-3.0 Hz and 1.5-2.5 Hz	Percentile for all Possible Rotations of Double Couple Sources	Largest Azimuthal Gap Between the Stations Used (^{o})	Number of Stations Used	Region
1	70/110/140	71.14	60/120/120	69.33	28	2	288	4	PQ
2	10/70/170	71.35	60/150/240	66.80	59	22	319	3	PQ
3	80/150/20	72.85	60/0/120	67.95	14	0	324	3	PQ
4	60/60/240	73.00	60/60/240	71.71	0	0	288	4	PQ
5	80/130/120	72.75	60/120/120	74.04	22	1	284	4	ME
6	60/150/20	71.67	--					4	MA
7	50/140/320	68.26	--					4	NC
8	30/120/290	64.92	60/120/300	60.95	32	4	158	5	NC
9	60/150/190	72.49	60/30/300	74.16	9	0	128	6	NC
10	50/220/160	60.19	60/210/150	51.98	13	0	137	6	WV
11	50/0/10	60.71	--					6	WV
12	40/50/120	64.78	--					2	VA
13	80/110/200	65.18	--					4	VA

14	80/80/280	53.95	30/150/180	51.13	24	2	187	3	VA
15	80/230/310	70.29	60/300/90	65.54	98	87	149	4	MO
16	40/140/150	53.88	30/120/330*	49.78				3	MO
17	50/20/150	53.14	60/30/140	40.68	21	1	225	3	AR
18	60/40/20	61.16	60/60/210	29.37	69	34	218	4	TN
19	40/140/240	56.85	60/60/0	50.36	8	0	164	4	MO
20	70/150/60	66.46	60/0/150*	65.10				3	MO
21	50/100/170	56.73	60/120/120	56.18	63	26	136	6	MO
22	50/60/330	57.18	30/60/330	52.19	21	1	223	5	AR
23	70/130/110	59.20	60/0/30*	56.82				6	AR
24	60/160/10	55.04	60/30/30	48.58	80	52	226	4	AR
25	60/20/260	70.87	60/30/90*	60.26				3	OK
26	10/100/70	65.49	--					2	OK
27	70/10/260	67.94	--					1	OK
28	40/110/300	65.80	--					2	OK

D^o, R^o, S^o refers to the dip, rake and strike angles in degrees. MVR is the modified variance reduction.

We also compared the fits of the synthetic envelopes to the observed envelopes when the waveform envelopes are filtered through the two different frequency bands of 1.0-3.0 Hz and 1.5-2.5 Hz and saw that for the most of the events analyzed in this study, the synthetic envelopes produce a better fit the observed envelope when the waveform envelopes are filtered through the frequency band of 1.0-3.0 Hz, indicating that the focal mechanisms obtained using 1.0-3.0 Hz are as well constrained as the focal mechanisms obtained using 1.5-2.5 Hz. The method of Dahal and Ebel (2019, 2020) has produced robust results for focal depths, moment magnitudes and focal mechanisms for the events with magnitudes M_w 3.7-2.7 for different geographical regions of the CEUS tested in this study. This study shows that the Dahal and Ebel (2019, 2020) method can be used to find accurate focal depths and seismic moments for events as small as M_w 2.7 in the CEUS, and in many cases it can find accurate focal mechanisms as well for such small events in the region. If applied widely to current and past events in the CEUS, this method can greatly improve the input parameters for seismic hazard analyses of the region.

DATA AND RESOURCES

Event origin time, station epicentral distance, station azimuth, station network code, event magnitude, station name and the seismograms were read from the IRIS wilber3 system (http://ds.iris.edu/wilber3/find_stations/10002986, last accessed June 2020). The focal depths and the magnitudes of the events reported from the earlier studies were primarily from the Advanced National Seismic System of the USGS (https://www.usgs.gov/natural-hazards/earthquake-hazards/earthquakes, last accessed June 2020) and from the Lamont-Doherty Earth Observatory website (https://www.ldeo.columbia.edu/research/seismology-geology-tectonophysics/earthquake-information, last accessed June 2020) and the website of the Natural Resources of Canada (https://earthquakescanada.nrcan.gc.ca/index-en.php, last accessed June 2020) whenever available. The crustal models in Table 4 and Table 5, and the focal mechanisms from previous studies whenever available, were taken from R. Herrmann's website (http://www.eas.slu.edu/eqc/eqc_mt/MECH.NA/, last accessed July 2020).

ACKNOWLEDGEMENTS

This report is based upon work supported by the U.S. Geological Survey under Grant No. G19AP00060. The authors are grateful to the USGS for this support. The authors also wish to thank the Academic Information Technology Department, Weston Observatory, and the Department of Earth and Environmental Sciences, all of Boston College, for providing the use of their facilities to support this research. The views and conclusions contained in this document are those of the authors and should not be interpreted as representing the opinions or policies of the U.S. Geological Survey.

REFERENCES

CEUS SSC (2012). *Technical Report: Central and Eastern United States Seismic Source Characterization for Nuclear Facilities*, EPRI Report #1021097, U.S. DOE Report # DOE/NE-0140.

Dahal, N. R., and J. E. Ebel (2019). Method for determination of depths and moment magnitudes of small-magnitude local and regional earthquakes recorded by a sparse seismic network, *Bull. Seismol. Soc. Am.* **109**, 124–137.

Dahal, N. R., and J. E. Ebel (2020). Method for Determination of Focal Mechanisms of Magnitude 2.5–4.0 Earthquakes Recorded by a Sparse Regional Seismic Network, *Bull. Seismol. Soc. Am.* **110**, 715–726

Dreger, D. S. (2008). Time-domain moment tensor INVerse Code (TDMT _INVC), available at ftp://ftp.geo.uib.no/pub/seismo/ SOFTWARE/SEISAN/OLDER_VERSIONS/SEISAN_10.4.1/ alpha/LINUX/INF/mt_dreger.pdf (last accessed March 2018).

Dreger, D. S., and D. V. Helmberger (1993), Determination of Source Parameters at Regional Distances with Single Station or Sparse Network Data, *J. Geophys. Res.* **98**, 8107-8125.

Duputel, Z., L. Rivera, Y. Fukahata, and H. Kanamori (2012). Uncertainty estimations for seismic source inversions, *Geophys. J. Int.* **190**, 1243– 1256, doi: 10.1111/j.1365-246X.2012.05554.x.

Ebel, J. E., M. C. Chapman, W.-Y. Kim, and M. Withers (2019). Current Status and Future of Regional Seismic Network Monitoring in the Central and Eastern United States, *Seismol. Res. Lett.* **91**, 660–676, doi: 10.1785/0220190210.

Guilhem, A., L. Hutchings, D.S. Dreger, and L.R. Johnson (2014). Moment tensor inversions of M ~ 3 earthquakes in the Geysers geothermal fields, California, *J. Geophys. Res.* **119**, 2121-2137, doi: 10.1002/2013JB010271.

Jost, M. L., and R. B. Herrmann (1989). A student's guide to and review of moment tensors, *Seismol. Res. Lett.* **60**, 37–57.

Kagan, Y. Y. (1992). Correlations of earthquake focal mechanisms, *Geophys. J. Int.* **110**, 305–320.

Saikia, C. (1994). Modified frequency-wavenumber algorithm for regional seismograms using Filon's quadrature: modelling of *Lg* waves in eastern North America, *Geophys. J. Int.* **118**, 142-158.

Wheeler, R.L., 2014, Earthquake catalog for estimation of maximum earthquake magnitude, Central and Eastern United States—Part B, Historical Earthquakes, *U.S. Geological Survey Open-File Report 2014– 1025–B*, 30 p., *http://dx.doi.org/10.3133/ofr20141025B*.

Zhao, L.S., and D.V. Helmberger (1994). Source estimation from broadband regional seismograms, *Bull. Seism. Soc. Am.*, **84**, 91-104.

Zhu, L., and D.V. Helmberger (1996). Advancement in source estimation techniques using broadband regional seismograms, *Bull. Seism. Soc. Am.* **86**, 1634-1641.